Ferroelectric Polarization in $BaTiO_3$ Nanocrystals controls Photoelectrochemical Water Oxidation and Photocatalytic Hydrogen Evolution

Samutr Assavachin, and Frank E. Osterloh*

Department of Chemistry, University of California, Davis, CA 95616, USA, fosterloh@ucdavis.edu

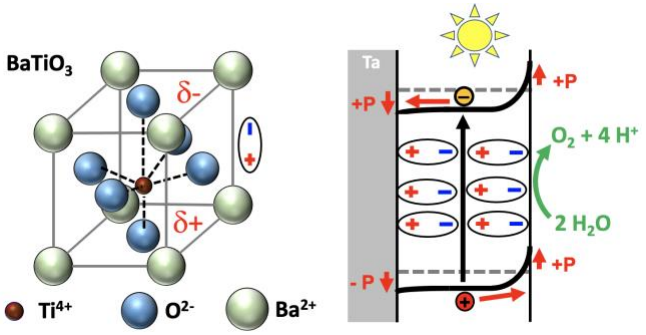

Abstract

Ferroelectric (FE) semiconductors such as $BaTiO_3$ support a remnant polarization after application of an electric field that can promote the separation of photogenerated charge carriers. Here we demonstrate FE-enhanced photocatalytic hydrogen evolution and photoelectrochemical water oxidation with barium titanate nanocrystals for the first time. Nanocrystals of the ferroelectric tetragonal structure type were obtained by hydrothermal synthesis from TiO_2 and barium hydroxide in 63% yield. $BaTiO_3$ nanocrystal films on tantalum substrates exhibit water oxidation photocurrents of 0.141 mA cm^{-2} at 1.23 V RHE under UV light (60 mW cm^{-2}) illumination. Electric polarization at 52.8 kV cm^{-1} increases the photocurrent by a factor of 2 or decreases it by a factor of 3.5, depending on the field orientation. It also shifts the onset potential by -0.15 V or +0.09 V, depending on the polarity of the applied field, and it modifies the surface photovoltage signal. Lastly, exposure to an electric field increases the H_2 evolution rate of Pt/$BaTiO_3$ by a factor of ~1.5 and it raises the selectivity of photodeposition of silver onto the (001) facets of the nanocrystal.

All FE enhancements can be removed by heating samples above the Curie temperature of $BaTiO_3$. These findings can be explained with FE dipole-induced changes to the potential drop across the space charge layer of the material. The ability to use the ferroelectric effect to enhance hydrogen evolution and water oxidation is of potential interest for the development of improved solar energy to fuel conversion systems.

INTRODUCTION

Ferroelectric (FE) materials exhibit a spontaneous electric polarization that can be reversed through application of an external electric field. The ferroelectric (FE) effect was discovered in 1920 in potassium sodium tartrate tetrahydrate (the Rochelle salt) by Joseph Valasek, and later in $BaTiO_3$ and other materials ($PbTiO_3$, $BiFeO_3$, $LiNbO_3$, $KNbO_3$). [1-3] In some compounds, such as $BiFeO_3$, the ferroelectric polarization is due to changes in bonding, [4] while in others, such as barium titanate, it is due to the displacement of a Ti(4+) ion from its equilibrium position (**Figure 1**). [5] In $BaTiO_3$, this ion shift occurs below the ferroelectric Curie Temperature (110-120°C) [6-8] and is accompanied by a change from the cubic to the tetragonal crystal structure.

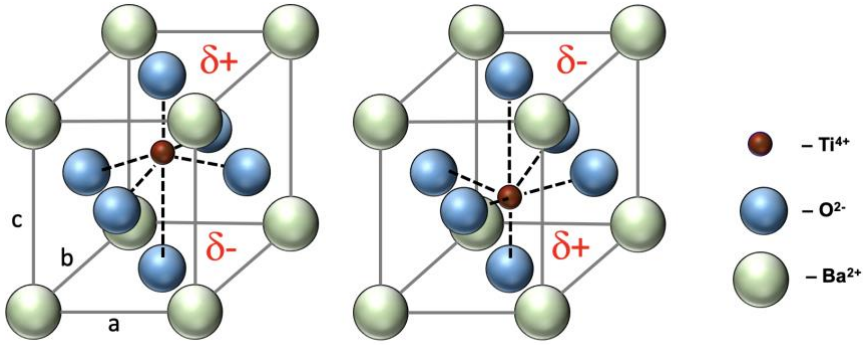

Figure 1. Unit cell of tetragonal $BaTiO_3$ with titanium center displacement leading to a ferroelectric dipole.

In ferroelectric semiconductors, the FE dipole may affect the direction of charge separation under illumination. [9-12] This can produce an anomalous (or bulk) photovoltaic effect, when the photovoltage exceeds the band gap of the semiconductor. [13] For example, ferroelectric $BiFeO_3$ films support photovoltages of 16 V and the short circuit currents densities of 0.12 mA cm^{-2} under certain conditions. [14] The high solar energy conversion efficiency of lead iodide perovskite photovoltaics ($CH_3NH_3PbI_3$) has also been attributed to an FE effect. [9, 15]

While the FE effect is well established in photovoltaics, there is less convincing proof for it in solar fuel photoelectrochemistry and photocatalysis.[10, 16-17] This is because photocatalysts for thermodynamically

unfavorable fuel forming reactions, such as the water splitting reaction, [18-19] are influenced by many factors, including polar surface terminations, surface recombination, and kinetic overpotentials. This makes it very difficult to attribute observed activity variations solely to ferroelectric effects. [20-23] Also, many ferroelectric materials with visible band gaps, incl. $BiFeO_3$ and $PbTiO_3$, are not stable under water electrolysis conditions. Some of these challenges can be avoided by focusing on dye degradation reactions,[21, 24-26] however, because photocatalytic dye degradation reactions are thermodynamically downhill ($\Delta G < 0$) they do not provide information about the energy conversion efficiency of the catalysts. [27-28] Another problem is that ferroelectric photoelectrodes are often polarized electrically in the presence of electrolytes and air, [29-31] where they may be changed as a result of oxidation/reduction reactions under these conditions. [32]

Some of the most direct evidence for FE-controlled photoelectrochemistry was obtained for $BaTiO_3$ crystals in Rohrer's group.[33-34] When the crystals are illuminated, reductive silver photodeposition takes place preferentially on the positive FE domains, while oxidative PbO_2 deposition occurs on the negatively charged domains. A similar reactivity was also observed in $BiVO_4$ phases after doping with Na and Mo [35] and in TiO_2 coated $BiFeO_3$. [36] This confirms that the FE dipole in these metal oxides can guide the direction of photogenerated charge carrier transport. Electrically polarized ferroelectric $BaTiO_3$ single crystals also have extended carrier lifetimes, [37] which was attributed to improved charge separation. In confirmation of this interpretation, the enhancement can be turned off by heating the crystal above the ferroelectric Curie Temperature T_C (110-120°C). [6-8] Very recently, Magnan et al. reported that $BaTiO_3$ films displayed electric polarization-dependent photocurrent for water oxidation. [32] However, doping during electrochemical polarization in electrolyte could not be ruled out. Similarly, Liu et al, reported FE-controlled reductive and oxidative photodeposition of Cr_2O_3 and MnO_x onto a gold-modified $BaTiO_3$ single crystal [38] Sub-micromolar amounts of H_2 and O_2 were detected when a Rh/Cr_2O_3 and CoOOH-modified $Au/BaTiO_3$ crystal was exposed to UV light, but it was not clear if gas evolution was catalytic and if it was promoted by a ferroelectric effect.

In continuation of our work on ferroelectric photocatalysts [39] we report here on the first observation of ferroelectrically enhanced photoelectrochemical water oxidation and hydrogen evolution with $BaTiO_3$ nanocrystals. Single crystals in the tetragonal ferroelectric form were obtained by hydrothermal reaction of TiO_2 and $Ba(OH)_2$. When the nanocrystals are deposited on tantalum substrates they are able to oxidize water to O_2 under UV illumination and with an applied bias. The photocurrent can be enhanced or suppressed reversibly through prior electric polarization of the films under inert conditions. A prior applied electric field also increases the photocatalytic H_2 evolution with Pt-modified $BaTiO_3$ nanocrystals by a factor of 1.5 and it directs photochemical silver deposition to the (001) facets. Importantly photocurrent and H_2 evolution activity are restored to their original value by heating the $BaTiO_3$ nanocrystals above their Curie temperature. These findings not only show that the photoelectrochemical properties of $BaTiO_3$ nanocrystals are controlled by a ferroelectric effect, but also that the effect can be utilized for the photoelectrochemical generation of H_2 fuel.

RESULTS AND DISCUSSION

The synthesis of $BaTiO_3$ was achieved by heating P25 TiO_2, $Ba(OH)_2$ and KOH in water to 180°C under hydrothermal conditions, similar to the published procedure. [40] After 72 h, the reaction is complete and provides barium titanate nanocrystals in 63% yield (based on TiO_2). According to SEM and TEM images in **Figure 2**, the crystals are 242 nm (±90.8 nm) in size (histogram in **Figure S1**). The morphology of the crystals is dominated by the ⟨100⟩ family of facets and about 90% of them appear tetragonal with one dimension expanded. Some of the crystals are truncated at the corners, exposing ⟨111⟩ facets there. The SAED pattern for a single nanocrystal in **Figure 2** shows a single set of reflections that can be indexed to the tetragonal lattice of $BaTiO_3$. This confirms that the nanocrystals are single crystals. The powder XRD pattern in **Figure 3** can be indexed to the tetragonal crystal structure of $BaTiO_3$.[41] Based on the absence of

any impurity peaks, the obtained material is phase-pure. Interestingly, the hydrothermal procedure by Tsumura et al. produces cubic $BaTiO_3$, which may be attributed to the lower synthesis temperature (150°C) compared to the conditions used here (180 °C). [40] The cubic to tetragonal transition temperature for $BaTiO_3$ is 120°C. [41] We also find that highly basic conditions are required to obtain a uniform product.

The $BaTiO_3$ particles are obtained as a white powder, consistent with the diffuse reflectance spectrum in **Figure 3b.** Based on the absorption onset, the band gap is found at 3.1 eV, near literature values (3.0-3.3 eV). [19, 42]

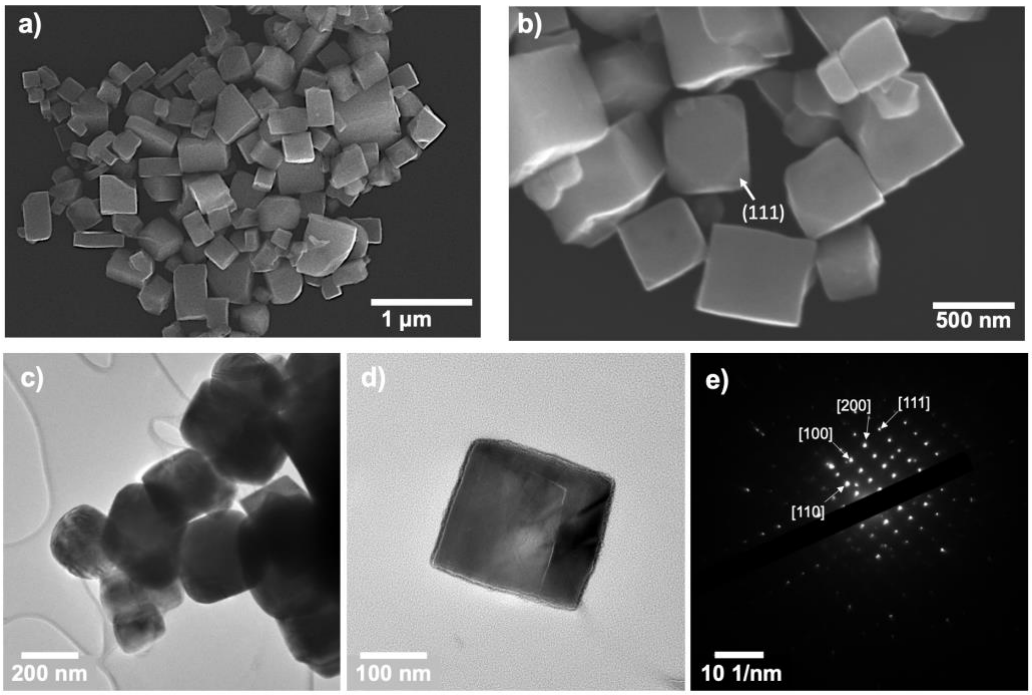

Figure 2. Electron micrographs of $BaTiO_3$. a,b) SEM images. c,d) TEM images. d) SAED pattern.

To evaluate the photoelectrochemical properties of the material, $BaTiO_3$ particle films were fabricated as shown in **Figure S2** by drop-coating a $BaTiO_3$ particle suspension in deionized water onto a precleaned (10% hydrofluoric acid) tantalum substrate. Tantalum was chosen because its low workfunction of 4.25 eV [43] favors an Ohmic contact with n-type $BaTiO_3$. The dried particle film was then treated with a 5 x 10 µL 20 mM $TiCl_4$ suspension in anhydrous methanol, followed by annealing at 600ºC in argon. This 'necking

method' produces a network of TiO_2 that enhances the conductivity in particle films.[44] Based on optical appearance and SEM images (**Figure 3c,d**), the resulting film is thin with most $BaTiO_3$ particles in direct contact with the Ta substrate.

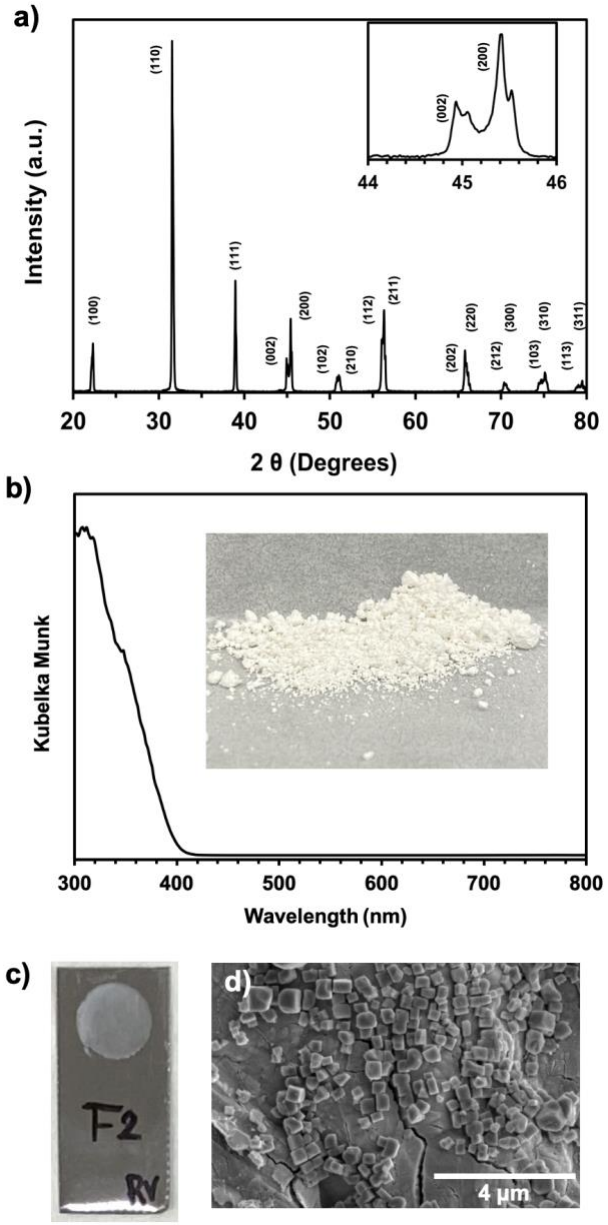

Figure 3. a) Powder XRD pattern of hydrothermal synthesized $BaTiO_3$. The pattern matches the **1507756** reference at the Crystallography Open Database (COD). The inset shows 002 and 200 peaks indicating the tetragonal crystal phase. Each reflection is split further, due to the splitting of the Cu-Kα emission, as reported previously. [45] b) Kubelka Munk spectrum of $BaTiO_3$ powder with photo as insert. c) Photo and d) SEM of $BaTiO_3$ film on tantalum.

The Ta/$BaTiO_3$ film was mounted inside of an electrochemical cell containing 0.5 M Na_2SO_4 aqueous solution (pH = 5.95, **Figure S3**), and used to record a linear sweep voltammogram under chopped UV light illumination (60 mW cm^{-2}) from a 300 W Xe lamp source (**Figure 4b**). The anodic photocurrent (0.141 mA cm^{-2} at 1.23 V RHE) is mainly from excitation of $BaTiO_3$ (**Figure S4**) and comparable to a previous literature report. [46] The current is stable over a 1.0 h period and due to water oxidation, as evidenced by the formation of gas bubbles (**Figure S8** and **movie** in Supporting Information).

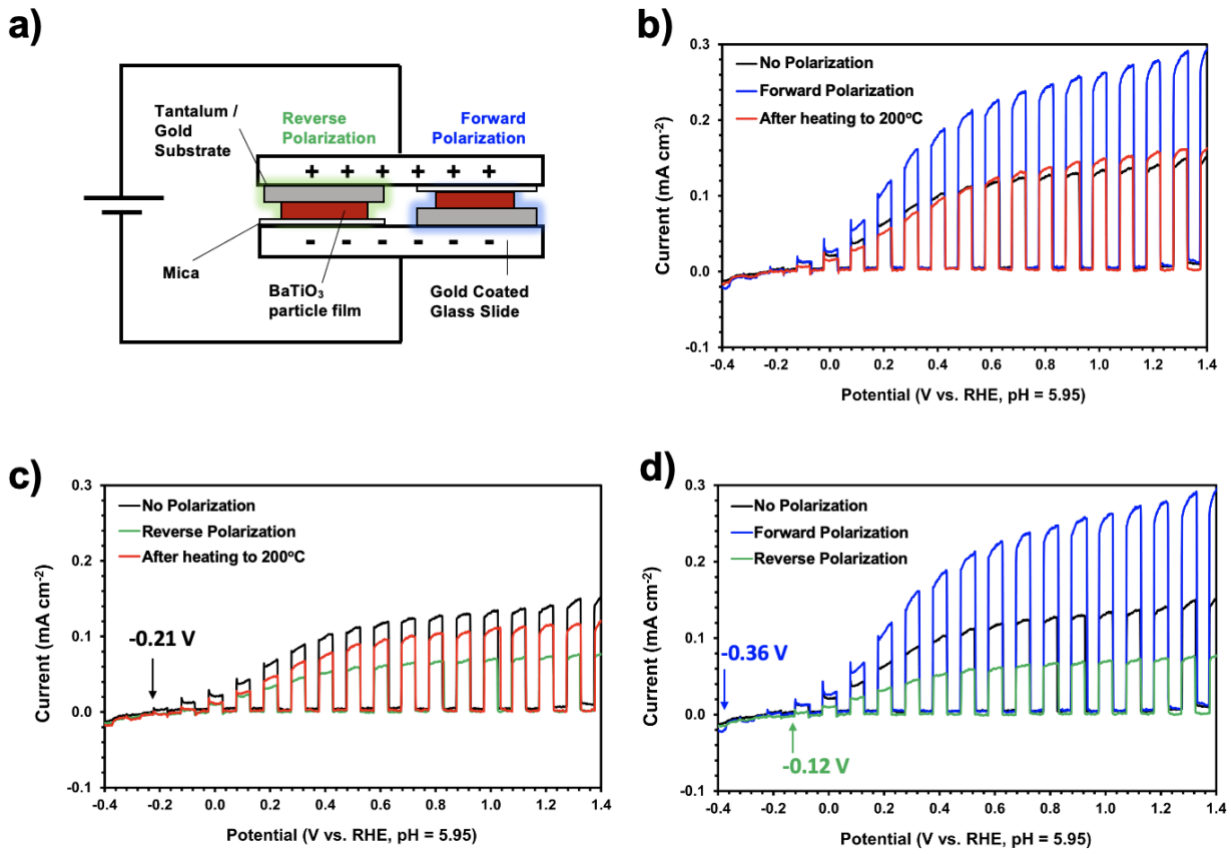

Figure 4. a) Polarization of the Ta/$BaTiO_3$ film at room temperature in high-purity argon atmosphere. In 'Forward polarization' the tantalum substrate was connected to the negative lead and in 'Reverse polarization' to the positive lead of the power supply. b) Photoelectrochemical scans of $BaTiO_3$ films before polarization, after Forward polarization, and after heating to 200°C in argon, c) before polarization, after Reverse polarization, and after heating to 200°C in argon, and d), before and after Forward or Reverse polarization. Photocurrent onset potentials E_{on} are shown as numerical values. Conditions: 0.5 M Na_2SO_4 aqueous solution (pH = 5.95) under chopped UV light illumination (60 mW cm^{-2}) from a 300 W Xe lamp source. Voltametric scans were conducted from negative to

positive applied potential. Repeat measurements on multiple samples and error analysis are presented in **Figure S5** and **Tables S6/S7**.

Overall, the current appears limited by the optical absorbance of the $BaTiO_3$ monolayer in the film. After the PEC scan, the Ta/$BaTiO_3$ film was removed, cleaned with deionized water, dried, and exposed to an electric field of 52.8 kV cm^{-1} for 1.0 h in *Forward Polarization* orientation as defined in **Figure 4a**. When the PEC scan was repeated, the photocurrent (0.276 mA cm^{-2} at 1.23 V RHE) increased by a factor of 1.95. The film was removed again, rinsed with water, and annealed at 200°C for 30 minutes in air to reset the polarization in $BaTiO_3$ (the FE Curie Temperature is 110-120°C for $BaTiO_3$).[6-8] When the PEC scan was repeated (**Figure 4b**), the anodic photocurrent (0.157 mA cm^{-2} at 1.23 V RHE) was nearly the same as observed for the non-polarized film. Next, the same film was rinsed, dried, and polarized in *Reverse Polarization* direction, and the PEC scan was repeated (**Figure 4c)**, to reveal a photocurrent of 0.073 mA cm^{-2} at 1.23 V RHE (decreased by a factor of 1.93 compared to the non-polarized film). Finally, the film was washed, dried, and heated to 200°C, as before, to yield the PEC response in **Figure 4c**, with a photocurrent (0.114 mA cm^{-2} at 1.23 V RHE), restored to 81% of the original value. Overall (**Figure 4d**), the Forward Polarization enhances the photocurrent by a factor of ~2 and reverse polarization diminishes it by the same factor. This behavior was reproducible with four additional films (**Figure S6**), resulting in a mean photocurrent increase of 1.97 ± 10.7% and decrease of 3.46 ± 28.3%, after *forward* and *reverse* polarization, respectively (**Figure S5** and **Table S6/S7**).

As can be seen from **Figures 4c** and **d**, polarization also shifts the photocurrent onset potential as follows: -0.36 V (Forward P.) < -0.21 (No P.) < -0.12 V (Reverse P.) for the respective films. This shows that the polarization also affects the photovoltage of the Ta/$BaTiO_3$/liquid junction. These results agree with

previous observations of anomalous photovoltages in ferroelectric $BaTiO_3$ thin films, [7-8] and suggest that the PEC behavior of $BaTiO_3$ nanocrystals is controlled by a ferroelectric effect.

The photoelectrochemical results can be explained with the energy diagram in **Figure 5** for the $Ta/BaTiO_3/H_2O$ configuration. Without applied polarization, the $BaTiO_3$ crystals forms a depletion layer at the solid-liquid interface and a near ohmic contact with the tantalum substrate. The depletion layer promotes hole transfer into the solution (photoanode behavior) and allows electrons to transfer into the Ta substrate. Electric polarization induces a ferroelectric (FE) dipole in $BaTiO_3$ that modifies the band bending near the particle interfaces (inside the material the FE dipoles cancel out). Forward polarization raises the solid-liquid band edge position by an amount P, thereby increasing the potential drop across the depletion layer, and promoting photohole transfer into the liquid (photoanode behavior). The FE dipole also lowers the band edge at the $Ta/BaTiO_3$ contact by the same amount P, to improve photoelectron transfer into the Ta substrate (photoanode behavior). Reverse polarization has the opposite effects (diminishes photoanode behavior). The size of the FE induced band shift P can be estimated from the photocurrent onset shift E_{ON}(Polarized)-E_{ON}(Non-Polarized) in the PEC scans in **Figure 4**. Accordingly, P = 0.15 eV for Forward polarization and 0.09 eV for Reverse polarization.

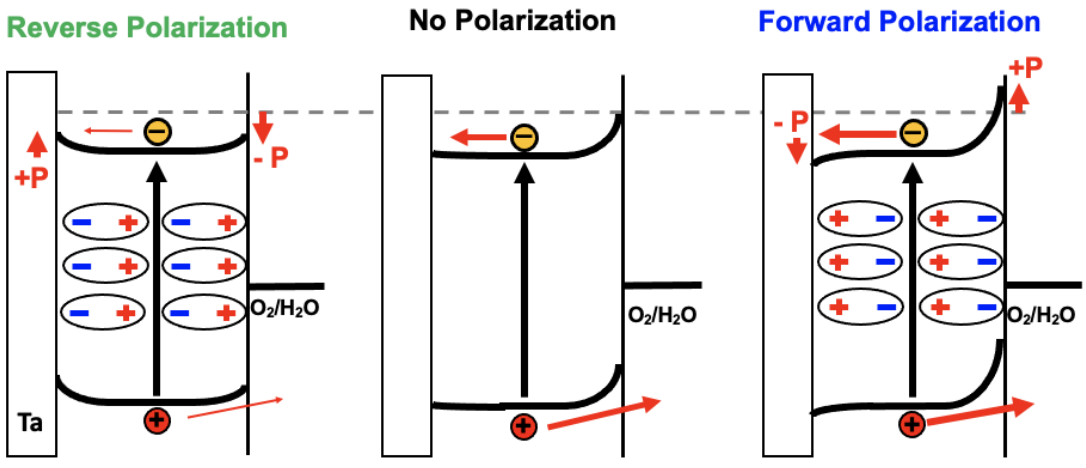

Figure 5. Effect of FE polarization on the photoelectrochemistry of $BaTiO_3$ /liquid contacts. +P and -P are the band energy shifts due to electric polarization.

To verify the model, Vibrating Kelvin Probe Surface photovoltage spectra (VKP-SPS) were recorded on $BaTiO_3$ particle films in vacuum. VKP-SPS measures the contact potential difference (CPD) of a sample with a commercially available vibrating Kelvin probe (Besocke Delta Phi, see insert in **Figure 6**). Illumination through the semi-transparent probe disturbs the distribution of the charge carriers in the sample and produces a surface photovoltage signal $SPV = CPD_{light} - CPD_{dark}$. The sign and size of the SPV signal provides information about the direction of charge separation and the driving force.[47-48] As can be seen from **Figure 6**, all $BaTiO_3$ particle films yield negative SPV signals at 3.2 eV, near the optical band gap of the material. This confirms that the SPV signal is generated by charge carrier movement in the depletion layer at the surface, as shown in **Figure 6a**. The SPV signal (-0.61 V) is largest for the forward polarized $BaTiO_3$ film, followed by the non-polarized film (-0.38 V) and the reverse polarized film (-0.23 V). This agrees with the photocurrent trend in **Figure 4**. It confirms that photochemical charge transfer in $BaTiO_3$ is predominantly controlled by the surface FE dipoles shown in **Figure 5**.

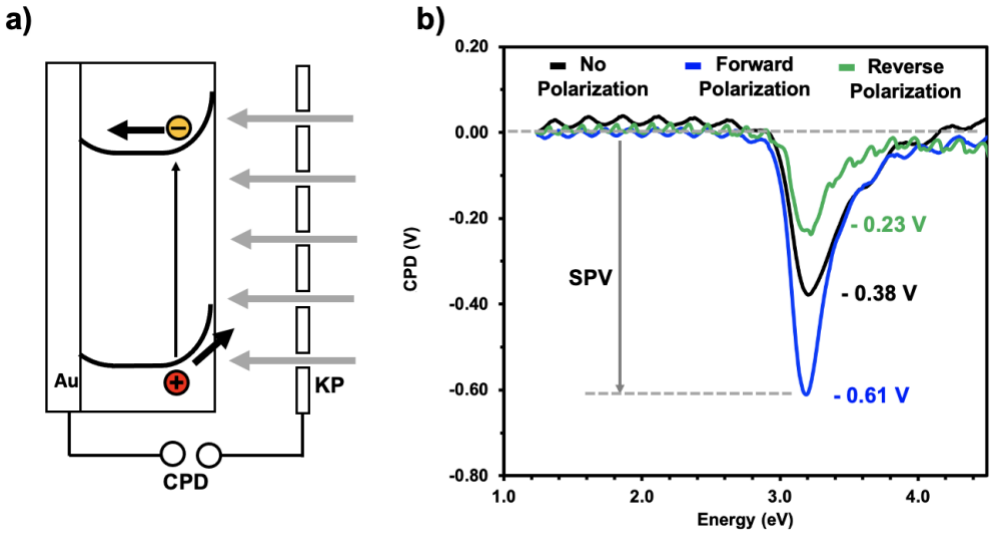

Figure 6. a) Surface photovoltage (SPV) measurement geometry and b) SPV spectra of $BaTiO_3$ particle film on gold substrate in vacuum, before and after electric polarization in a 52.8 kV/cm field. For detailed measurement configuration see **Figure S10**.

To test if the FE polarization can be used to also control photocatalytic hydrogen evolution with a $BaTiO_3$

particle suspension, polarization experiments were carried out on the $BaTiO_3$ powder. For this purpose, 100 mg of dry $BaTiO_3$ powder was sandwiched between two mica crystals and subjected to a 6.32 kV/cm electric field for 1.0 h, as shown in **Figure S9**. Platinum cocatalyst was then deposited onto the freshly polarized $BaTiO_3$ powder, by irradiating it with UV light in the presence of 0.1% mass (based on $BaTiO_3$ weight) hexachloroplatinic acid and 20% aqueous methanol as sacrificial electron donor. Platinum photodeposition began immediately as indicated by a color change of the suspension from white to slightly grey.

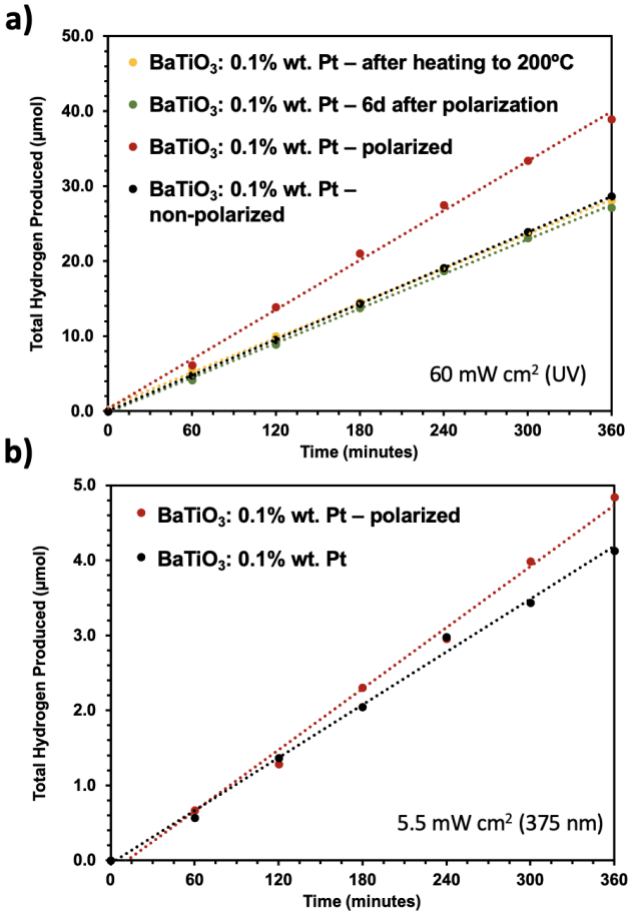

Figure 7. H_2 evolution from 100 mg of 0.1%wt Pt – loaded $BaTiO_3$ in 100 mL of 20% (vol) aqueous methanol under a) 60 mW/cm^2 UV light irradiation, b) under 375 nm LED illumination (5.5 mW cm^{-2}; illumination area is 2.01 cm^2). The Apparent Quantum Yield (AQY) is 1.12 % for the non-polarized and 1.29 % for the polarized material.

Illumination was continued for 6 hours under 60 mW/cm^2 UV light to observe H_2 evolution (**Figure 7**) at a

constant rate of 6.49 μmol/h. Under 375 nm LED illumination (**Figure 7b**), the rate was 0.81 μmol/h, corresponding to an apparent quantum yield (AQY) of 1.29%. In comparison, the H_2 production rate of a Pt/$BaTiO_3$ sample prepared without prior electric polarization, was only 4.77 μmol/h (AQY of 1.12 % at 375 nm, rate = 0.69 μmol/h). These observations were reproducible in three separate batches of $BaTiO_3$ (**Figure S11** and **Table S12**). Based on this data, electric polarization enhances the H_2 evolution activity 1.53 times compared to a non-polarized sample. While the absolute activities are low, they are comparable to an earlier report. [19]

Lastly, to determine the effect of heat treatment on the FE polarization, another fresh sample of polarized $BaTiO_3$ was heated to 200°C in air for 20 min prior to Pt photodeposition. As expected, the annealed $BaTiO_3$ shows a hydrogen production rate of 4.68 μmol/h, almost identical to the non-polarized material (**Figure 7a**). Overall, the results in **Figure 7** confirm that the photocatalytic activity can be aided by electric polarization and removed by annealing above the Curie temperature, as expected from the theory.

Because the amount of photodeposited platinum in the Pt/$BaTiO_3$ photocatalyst particles was too small for imaging, silver photolabeling was employed to determine the effect of the FE on charge separation in the $BaTiO_3$ particles. [33] For the experiment, $BaTiO_3$ powders were suspended in 0.1 M $AgNO_3$ solution and illuminated with 10 mW cm^{-2} UV light for 2 minutes. Photodeposition of silver occurred over the course of seconds, as indicated by a grey color appearance of the suspension. Particles were removed, washed and then imaged by SEM. As can be seen in **Figure 8**, polarization changes both the sizes and locations of the photodeposited silver particles. For non-polarized $BaTiO_3$, silver particles are 28.8 ±10.6 nm (n=44) in size and grow randomly on all facets of the $BaTiO_3$ crystals (see also **Figure S13)**. For polarized $BaTiO_3$, on the other hand, the silver particles are smaller (22.5 ± 14.4 nm, n = 94) and located predominantly on the (001) facets.

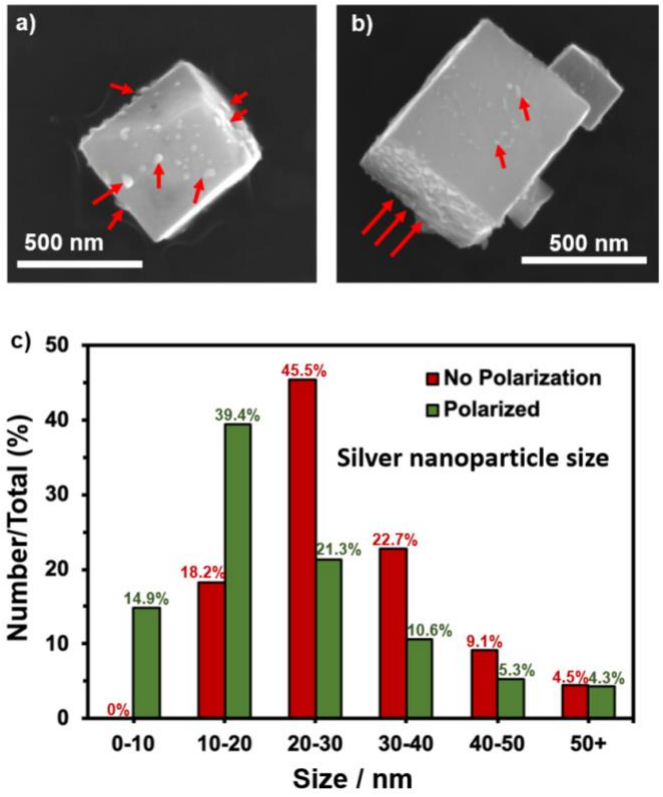

Figure 8. SEM images of $Ag/BaTiO_3$ after photodeposition of 1% wt. Ag from $AgNO_3$ in 20% aqueous methanol suspension with 10 mW/cm^2 UV light irradiation in 2 minutes. a) Non-polarized $BaTiO_3$ particles. b) $BaTiO_3$ particles polarized at 6.32 kV/cm for 1 hour. c) Ag nanoparticle size distribution from SEM.

These observations can be explained with the model in **Figure 9**. $BaTiO_3$ nanocrystals that were polarized along the c-axis (the axis of polarization) are expected to shift their bands as in **Figure 5**, allowing for accumulation of holes and electrons on opposing (001) facets. This explains the observation of increased H_2 evolution activity in **Figure 7** and the facet-selective silver deposition in **Figure 8**. The smaller size and greater number of (001) facet photodeposited Ag particles can be understood on the basis of Nucleation Theory. [49] The more reducing the electrochemical potential, the smaller the critical nucleation radius, and the smaller and more numerous the Ag particles. Non-polarized $BaTiO_3$ particles, on the other hand, do not have designated electron accumulation site and therefore the Ag particles are larger and fewer. Because the ferroelectric Ti^{4+} displacement in $BaTiO_3$ occurs only along the c-axis (**Figure 1**), particles exposed to an

electric field along the a or b axis *cannot* develop a FE polarization. These particles will behave like $BaTiO_3$ particles that were never exposed to an electric field, or like particles that were heated to above their Curie temperature. The non-polarized particles may still have FE domains, but their size is smaller and the dipoles in adjacent domains cancel each other, resulting in a net zero polarization. This explains the lower proton reduction rate and the lower facet selectivity for Ag deposition.

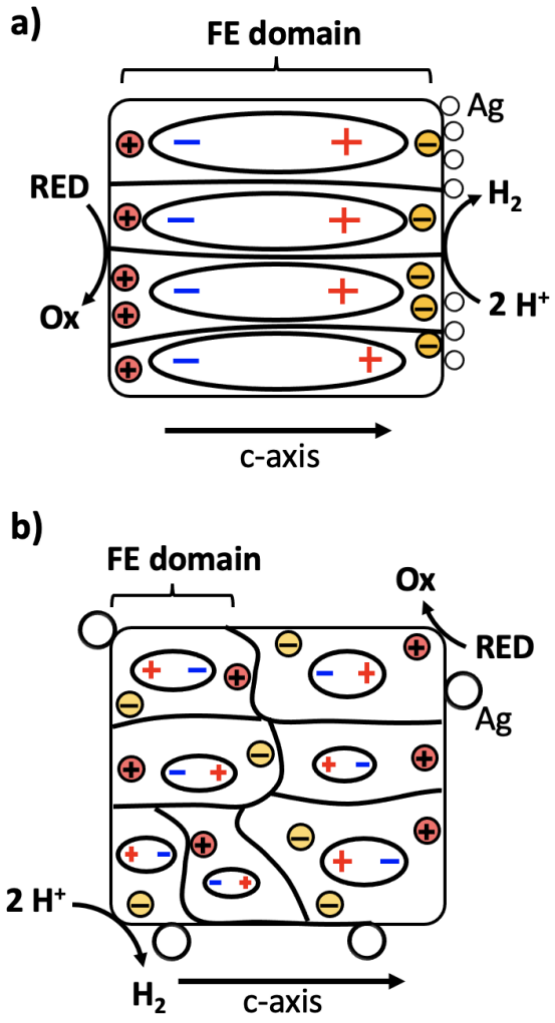

Figure 9. FE domain model for $BaTiO_3$ particles. a) large, oriented FE domains form after electric polarization along the c-axis. Increased FE domain size improves photocatalytic H_2 evolution activity / photochemical silver deposition. b) small, non-oriented FE domains are present after electric field polarization perpendicular to the c-axis, or after particles are heated to above their Curie temperature T_C.

The model in **Figure 9** also explains the relatively modest increase in water oxidation and H_2 evolution activity after electric field exposure. First of all, the $BaTiO_3$ nanocrystals are small (average 242 nm), which limits the number and the size of oriented FE domains and the corresponding photovoltage from them. [7, 14] Furthermore, because the $BaTiO_3$ crystals are randomly oriented in the electric field, only up to 33% of them (particles with the c-axis aligned with the field) can develop a polarization. This limits the overall FE enhancement that can be expected in the sample. The greater activity increase (factor of 2) seen for the $BaTiO_3$ photoelectrodes is attributed to the higher electric field (52.8 kV cm^{-1}) acting on the thinner film compared to the powdered sample (6.32 kV cm^{-1}). Overall, the models in **Figure 5** and **9** provide an explanation for the observed reactivity trends in $BaTiO_3$ films and $Pt/BaTiO_3$ photocatalysts.

Lastly, to evaluate the lifetime of the polarization, repeat PEC measurements were conducted 3 and 6 days after the initial polarization (**Figure S16**). The data shows that the 98 % of the polarization enhancement (100% of the suppression) is retained in samples stored in ambient conditions for 3 days. However, after 6 days the effect disappears completely and the photocurrent of both *Forward* and *Reverse* polarized samples returns to 82% of the value for the non-polarized samples. The detailed reasons for the quenching are not clear, although we hypothesize that the small size of the $BaTiO_3$ nanocrystals (diameter of 242 nm) restricts the size and stability of the FE domains. In $BaTiO_3$ single crystals, FE domains can exceed 15 μm in size, [33] while the lower size limit for FE domains is seen in 5 nm $BaTiO_3$ films. [50] Planned studies on the size-dependence of the FE polarization in $BaTiO_3$ crystals will bring further insight into this issue.

CONCLUSION

In summary, we demonstrate that prior electric polarization controls the photoelectrochemical water oxidation ability and photovoltage of nanosized tetragonal $BaTiO_3$ single crystals and their photocatalytic H_2 evolution activity in aqueous methanol. Both, activity enhancement and reduction can be observed,

depending on the polarity of the applied electric field. Heating the material above the ferroelectric Curie temperature removes polarization effects and restores the original activity. The modulation of the photoelectrochemistry can be explained with FE dipole-induced changes of the potential drop in the depletion layer of the $BaTiO_3$-liquid and Ta/$BaTiO_3$ junctions. The FE dipole modifies the photovoltage of the junctions by +0.15 V or -0.09 V, depending on the electric field direction during polarization. This increases the photocurrent by a factor of 2.0 ± 0.21, or diminishes it by a factor of 3.5 ± 0.98 respectively, relative to a non-polarized film, and it raises the photocatalytic H_2 evolution activity 1.53 times. Fundamentally, the size of the observed effect is limited by the random orientation of the $BaTiO_3$ nanocrystals in the homogeneous electric field. Because the electric polarization in $BaTiO_3$ is restricted to its crystallographic c-axis (the easy axis), no more than one third of the nanocrystals can be polarized. The stability of the polarization is limited to 3 days, which is attributed to the small size of the nanocrystals. Potentially, these problems may be overcome by growing $BaTiO_3$ films with preferred crystallographic orientation, and by synthesizing larger $BaTiO_3$ crystals which could support a greater number of FE domains.

EXPERIMENTAL SECTION

Barium hydroxide ($Ba(OH)_2$, 98 % Acros Organics),), titanium (IV) oxide (Aeroxide P25, Acros Organics), potassium hydroxide (KOH 99.9%, Sigma Aldrich). Water was purified to 18 MΩcm resistivity using a Nano-pure system. Titanium (IV) chloride ($TiCl_4$, 99.9% Acros Organics), anhydrous methanol (CH_3OH, 99.9% Alfa Aesar), gold-coated glass (Thermo Scientific), tantalum foil (99.95% metal basis, Alfa Aesar), hydrofluoric acid (HF, 48-51% solution in water, Acros Organics), muscovite mica (25x25mm, thickness 0.26-0.31mm, Electron Microscopy Sciences), sodium sulfate (Na_2SO_4, ≥99.0% Sigma Aldrich), hexachloroplatinate (IV) hexahydrate (99.9%, Alfa Aesar).

Barium titanate nanoparticles were synthesized with a hydrothermal reaction where 15 mmol (4.7319 g) barium hydroxide octahydrate, 14.3 mmol (1.14 g) P25 titanium dioxide, 0.30 mol (16.83 g) potassium hydroxide, and 30 mL of nanopure water are mixed and transferred into a 45 mL PTFE lined autoclave. The autoclave is then sealed and heated in an oven at 180°C for 72 hours. After cooling to room temperature, the white precipitate is washed with 1.0 M hydrochloric acid three times and then water to remove unreacted starting materials, and dried in air. Yield = 63 %.

Barium titanate particle films were obtained by drop coating 80 μL of 24 mg/mL $BaTiO_3$ aqueous suspension onto either a pre-cleaned gold substrate or pre-cleaned tantalum substrate covered with polyester masking tape (hole diameter = 0.8 cm). The $BaTiO_3$ aqueous suspension was sonicated for 10 minutes prior to drop coating. Gold substrates were cleaned in 30% hydrogen peroxide and potassium hydroxide solution for 1 minute, then acetone for 30 minutes, and washed with nanopure water and dried in air. The tantalum substrate was cleaned with 10% hydrofluoric acid aqueous solution for 10 minutes (Caution: Toxic, Corrosive) and then washed with anhydrous methanol. For the gold substrate, the drop-coated film was left to dry in air in the dark overnight before being annealed in argon at 450°C for 120 minutes, with a ramp rate of 2°C/min. The obtained film thickness is approximately 3.0 μm. For the tantalum substrate, necking

treatment was accomplished by adding 5 x 10 μL of 20 mM $TiCl_4$ in anhydrous methanol, followed by 30 min drying in air before annealing in argon at 600°C for 120 minutes, at a ramp rate of 2°C/min.

Kubelka-Munk optical spectra were recorded on a barium titanate powder pellet (3 g) using a Thermo Scientific Evolution 220 Spectrometer equipped with an integrating sphere. A barium sulfate standard was used to obtain a diffuse reflectance background.

Electrical polarization of particle films and powders was accomplished using the geometry in **Figure S9** and using sequence shown in **Figure S14** and **S15**. The particle film was sandwiched between two 2 x 4 cm^2 gold coated glass slides covered by Muscovite mica crystals (≤65 μm thick) for electrical insulation. The sandwich was then placed inside a quartz tube with continuous argon gas purging (1.0 L min^{-1}) and connected to a DC voltage source. Voltages of 79 V and 359 V were applied to the $BaTiO_3$ powder and the Ta/$BaTiO_3$ photoelectrode, respectively, for one hour at room temperature. The DC voltage was produced with a DC-HVDC Converter, FS Series, XP Power ® and measured with a digital multimeter using a voltage divider consisting of 0.499 MΩ and 49.3 kΩ resistors in series. Based on the electrode distance (0.0068 cm), the electric field for polarization was 52.8 kV cm^{-1} for the Ta/$BaTiO_3$ photoelectrode and 6.32 kV cm^{-1} for the $BaTiO_3$ powder (0.0125 cm electrode distance). Heating was performed in air for 30 minutes at 200°C, above the Curie Temperature (110-120°C), by placing samples into a preheated oven.

Photoelectrochemistry measurements were conducted using a Gamry Reference 600 Potentiostat connected to a three-electrode system consisting of the working electrode, a calomel reference electrode (3.5 M KCl), and a Pt counter electrode in 0.5 M Na_2SO_4 aqueous electrolyte solution (pH = 5.95). Chopped light linear sweep scans were accomplished with UV-light illumination from a 300W Xe lamp source with an intensity of 60 mW/cm^2 at the sample (**Figure S3**). The chopped light scan interval was 5 seconds with scan rate of 10 mV/s and scan step of 1 mV. Calibration was performed with $K_{3/4}[Fe(CN)_6]$ and using fluorine doped tin oxide (FTO) as the working electrode. All potentials were converted to RHE where RHE

= NHE + pH x 0.059V. The one-hour PEC experiment in **Figure S8** was performed using light from a 200 W Hg lamp.

Surface Photovoltage Spectroscopy (SPS) measurements were accomplished using a vibrating gold mesh Kelvin probe (Delta PHI Besocke) mounted inside a vacuum chamber held at 1.0 x 10^{-4} bar. The sample was mounted as shown in **Figure S10** with an alligator clip back contact and the Kelvin probe was positioned ~1 mm over the film surface. Samples were left to equilibrate until a stable baseline is obtained. The CPD signal was recorded in the 10,000 – 40,000 cm^{-1} interval using 100 cm^{-1} illumination increments every 5 seconds. A 300 W Xe lamp served as the light source.

Photochemical H_2 evolution measurements were accomplished by dispersing 100 mg of 0.1% wt. Pt/$BaTiO_3$ photocatalyst in 100 mL of 20% aqueous methanol solution at neutral pH. Irradiation was performed in a round bottom quartz flask using a 300 W Xe arc lamp with UV intensity at the flask of 60 mW cm^{-2}. The quartz flask was connected to a gas chromatograph (Varian 3800) by an air-tight circulation system that allowed the sample flask to be evacuated and purged with argon before taking measurements. Photodeposition of the platinum co-catalyst was performed by adding chloroplatinic acid to the reaction solution (0.1 mg in 100 mL) and irradiated with UV light for 10 minutes to ensure complete deposition. Data collection was performed every hour over a 6-hour period. Electric polarization experiments were performed in the sequence shown in **Figure S15.**

Photochemical silver deposition was accomplished by adding 1% weight $AgNO_3$ to a 20 mg $BaTiO_3$ 20% aqueous methanol suspension (20 mL) and by illuminating with UV light (Xe lamp, 20 mW/cm^2) for 2 minutes.

Acknowledgement

We thank the National Science Foundation for financial support (grant CHE 1900136) of this work. Support for surface photovoltage spectroscopy measurements was provided by the U.S. Department of Energy, Office of Science, Office of Basic Energy Sciences under Award Number DOE-SC0015329.

Supporting Information

Particle size histograms, experimental schemes, photocurrent and H_2 evolution data, statistical error calculations, a photo of the electrochemical setup, and scanning electron micrographs.

References

1. Valasek, J., Piezo-Electric and Allied Phenomena in Rochelle Salt. *Physical Review* **1921,** *17* (4), 475-481.

2. Martin, L. W.; Rappe, A. M., Thin-film ferroelectric materials and their applications. *Nature Reviews Materials* **2016,** *2*, 16087.

3. Ahn, C. H.; Rabe, K. M.; Triscone, J.-M., Ferroelectricity at the Nanoscale: Local Polarization in Oxide Thin Films and Heterostructures. *Science* **2004,** *303* (5657), 488-491.

4. Neaton, J. B.; Ederer, C.; Waghmare, U. V.; Spaldin, N. A.; Rabe, K. M., First-principles study of spontaneous polarization in multiferroic BiFeO3. *Phys. Rev. B* **2005,** *71* (1), 014113.

5. Merz, W. J., Domain Formation and Domain Wall Motions in Ferroelectric BaTiO3 Single Crystals. *Physical Review* **1954,** *95* (3), 690-698.

6. Merz, W. J., Double Hysteresis Loop of BaTiO3 at the Curie Point. *Physical Review* **1953,** *91* (3), 513-517.

7. Käppler, W.; Arlt, G., Photovoltaic effect in pure and modified barium titanate ceramics. *physica status solidi (a)* **1981,** *63* (2), 475-480.

8. Brody, P. S., Large polarization-dependent photovoltages in ceramic BaTiO3 + 5 wt.% CaTiO3. *Solid State Communications* **1973,** *12* (7), 673-676.

9. Butler, K. T.; Frost, J. M.; Walsh, A., Ferroelectric materials for solar energy conversion: photoferroics revisited. *Energ. & Environ. Sci.* **2015,** *8* (3), 838-848.

10. Lopez-Varo, P.; Bertoluzzi, L.; Bisquert, J.; Alexe, M.; Coll, M.; Huang, J.; Jimenez-Tejada, J. A.; Kirchartz, T.; Nechache, R.; Rosei, F.; Yuan, Y., Physical aspects of ferroelectric semiconductors for photovoltaic solar energy conversion. *Phys. Rep.* **2016,** *653*, 1-40.

11. Yuan, G.-L.; Wang, J., Evidences for the depletion region induced by the polarization of ferroelectric semiconductors. *Applied Physics Letters* **2009,** *95* (25), 252904.

12. Nechache, R.; Harnagea, C.; Li, S.; Cardenas, L.; Huang, W.; Chakrabartty, J.; Rosei, F., Bandgap tuning of multiferroic oxide solar cells. *Nature Photonics* **2015,** *9* (1), 61-67.

13. Fan, D.; Zhu, J.; Wang, X.; Wang, S.; Liu, Y.; Chen, R.; Feng, Z.; Fan, F.; Li, C., Dual Extraction of Photogenerated Electrons and Holes from a Ferroelectric Sr0.5Ba0.5Nb2O6 Semiconductor. *ACS Appl. Mater. Interfaces* **2016,** *8* (22), 13857-13864.

14. Yang, S. Y.; Seidel, J.; Byrnes, S. J.; Shafer, P.; Yang, C. H.; Rossell, M. D.; Yu, P.; Chu, Y. H.; Scott, J. F.; Ager, J. W.; Martin, L. W.; Ramesh, R., Above-bandgap voltages from ferroelectric photovoltaic devices. *Nature Nanotechnology* **2010,** *5* (2), 143-147.

15. Kutes, Y.; Ye, L.; Zhou, Y.; Pang, S.; Huey, B. D.; Padture, N. P., Direct Observation of Ferroelectric Domains in Solution-Processed CH3NH3PbI3 Perovskite Thin Films. *J. Phys. Chem. Lett.* **2014,** *5* (19), 3335-3339.

16. Li, Y.; Li, J.; Yang, W. G.; Wang, X. D., Implementation of ferroelectric materials in photocatalytic and photoelectrochemical water splitting. *Nanoscale Horizons* **2020,** *5* (8), 1174-1187.

17. Yu, Y.; Wang, X., Piezotronics in Photo-Electrochemistry. *Adv. Mater.* **2018,** *30* (43), 1800154.

18. Takata, T.; Jiang, J.; Sakata, Y.; Nakabayashi, M.; Shibata, N.; Nandal, V.; Seki, K.; Hisatomi, T.; Domen, K., Photocatalytic water splitting with a quantum efficiency of almost unity. *Nature* **2020,** *581* (7809), 411-414.

19. Maeda, K., Rhodium-Doped Barium Titanate Perovskite as a Stable p-Type Semiconductor Photocatalyst for Hydrogen Evolution under Visible Light. *ACS Appl. Mater. Interfaces* **2014,** *6* (3), 2167-2173.

20. Li, L.; Salvador, P. A.; Rohrer, G. S., Photocatalysts with internal electric fields. *Nanoscale* **2014,** *6* (1), 24-42.

21. Khan, M. A.; Nadeem, M. A.; Idriss, H., Ferroelectric polarization effect on surface chemistry and photo-catalytic activity: A review. *Surf. Sci. Rep.* **2016,** *71* (1), 1-31.

22. Inoue, Y.; Okamura, M.; Sato, K., A thin-film semiconducting titanium dioxide combined with ferroelectrics for photoassisted water decomposition. *J. Phys. Chem. C.* **1985,** *89* (24), 5184-5187.

23. Deng, J.; Banerjee, S.; Mohapatra, S. K.; Smith, Y. R.; Misra, M., Bismuth Iron Oxide Nanoparticles as Photocatalyst for Solar Hydrogen Generation from Water. *Journal of Fundamentals of Renewable Energy and Applications* **2011,** *1*, 10.

24. Senthilkumar, P.; Jency, D. A.; Kavinkumar, T.; Dhayanithi, D.; Dhanuskodi, S.; Umadevi, M.; Manivannan, S.; Giridharan, N. V.; Thiagarajan, V.; Sriramkumar, M.; Jothivenkatachalam, K., Built-in Electric Field Assisted Photocatalytic Dye Degradation and Photoelectrochemical Water Splitting of Ferroelectric Ce Doped BaTiO3 Nanoassemblies. *ACS Sustainable Chemistry & Engineering* **2019,** *7* (14), 12032-12043.

25. Cao, D.; Wang, Z.; Nasori; Wen, L.; Mi, Y.; Lei, Y., Switchable Charge-Transfer in the Photoelectrochemical Energy-Conversion Process of Ferroelectric BiFeO3 Photoelectrodes. *Angewandte Chemie* **2014,** *126* (41), 11207-11211.

26. Cui, Y.; Briscoe, J.; Dunn, S., Effect of Ferroelectricity on Solar-Light-Driven Photocatalytic Activity of BaTiO3—Influence on the Carrier Separation and Stern Layer Formation. *Chemistry of Materials* **2013,** *25* (21), 4215-4223.

27. Osterloh, F. E., Photocatalysis versus Photosynthesis: A Sensitivity Analysis of Devices for Solar Energy Conversion and Chemical Transformations. *ACS Energy Letters* **2017**, 445-453.

28. Bae, S.; Kim, S.; Lee, S.; Choi, W., Dye decolorization test for the activity assessment of visible light photocatalysts: Realities and limitations. *Catalysis Today* **2014,** *224*, 21-28.

29. Yang, W.; Yu, Y.; Starr, M. B.; Yin, X.; Li, Z.; Kvit, A.; Wang, S.; Zhao, P.; Wang, X., Ferroelectric Polarization-Enhanced Photoelectrochemical Water Splitting in TiO2–BaTiO3 Core–Shell Nanowire Photoanodes. *Nano Lett.* **2015,** *15* (11), 7574-7580.

30. Park, S.; Lee, C. W.; Kang, M.-G.; Kim, S.; Kim, H. J.; Kwon, J. E.; Park, S. Y.; Kang, C.-Y.; Hong, K. S.; Nam, K. T., A ferroelectric photocatalyst for enhancing hydrogen evolution: polarized particulate suspension. *Physical Chemistry Chemical Physics* **2014,** *16* (22), 10408-10413.

31. Fu, Q.; Wang, X.; Li, C.; Sui, Y.; Han, Y.; Lv, Z.; Song, B.; Xu, P., Enhanced photocatalytic activity on polarized ferroelectric KNbO3. *RSC Advances* **2016,** *6* (110), 108883-108887.

32. Magnan, H.; Deleuze, P. M.; Brehin, J.; Plays, T.; Stanescu, D.; Flavell, W. R.; Silly, M. G.; Domenichini, B.; Barbier, A., Tuning the Charge Carriers Migration in Epitaxial BaTiO3 Thin-Film Photoanodes. *J. Phys. Chem. C* **2020,** *124* (19), 10315-10323.

33. Giocondi, J. L.; Rohrer, G. S., Spatially selective photochemical reduction of silver on the surface of ferroelectric barium titanate. *Chemistry of Materials* **2001,** *13* (2), 241-242.

34. Giocondi, J. L.; Rohrer, G. S., Spatial Separation of Photochemical Oxidation and Reduction Reactions on the Surface of Ferroelectric BaTiO3. *J. Phys. Chem. B* **2001,** *105* (35), 8275-8277.

35. Munprom, R.; Salvador, P. A.; Rohrer, G. S., Ferroelastic domains improve photochemical reactivity: a comparative study of monoclinic and tetragonal (Bi1−0.5xNa0.5x)(V1−xMox)O4 ceramics. *J. Mater. Chem. A* **2016,** *4* (8), 2951-2959.

36. Zhang, Y.; Schultz, A. M.; Salvador, P. A.; Rohrer, G. S., Spatially selective visible light photocatalytic activity of TiO2/BiFeO3 heterostructures. *Journal of Materials Chemistry* **2011,** *21* (12), 4168-4174.

37. Morris, M. R.; Pendlebury, S. R.; Hong, J.; Dunn, S.; Durrant, J. R., Effect of Internal Electric Fields on Charge Carrier Dynamics in a Ferroelectric Material for Solar Energy Conversion. *Adv. Mater.* **2016,** *28* (33), 7123-7128.

38. Liu, Y.; Zhang, M.; Wang, Z.; He, J.; Zhang, J.; Ye, S.; Wang, X.; Li, D.; Yin, H.; Zhu, Q.; Jing, H.; Weng, Y.; Pan, F.; Chen, R.; Li, C.; Fan, F., Bipolar charge collecting structure enables overall water splitting on ferroelectric photocatalysts. *Nat. Commun.* **2022,** *13* (1), 4245.

39. Assavachin, S.; Nail, B. A.; V. Goncalves, R.; Mulcahy, J. R.; Lloyd, S. E.; Osterloh, F. E., Ferroelectric surface photovoltage enhancement in chromium-doped SrTiO3 nanocrystal photocatalysts for hydrogen evolution. *Materials Advances* **2020,** *1* (5), 1382-1389.

40. Tsumura, T.; Matsuoka, K.; Toyoda, M., Formation and Annealing of BaTiO3 and SrTiO3 Nanoparticles in KOH Solution. *J. Mater. Sci. & Tech.* **2010,** *26* (1), 33-38.

41. Evans, H., Jnr, An X-ray diffraction study of tetragonal barium titanate. *Acta Crystallographica* **1961,** *14* (10), 1019-1026.

42. Maruska, H. P.; Ghosh, A. K., Photocatalytic Decomposition of Water at Semiconductor Electrodes. *Sol. Energy* **1978,** *20* (6), 443-458.

43. Michaelson, H. B., Electron Work Function of the Elements. In *CRC Handbook of Chemistry and Physics*, 88 (Internet Version 2008) ed.; Lide, D. R., Ed. CRC Press/Taylor and Francis: Boca Raton, FL, 2008.

44. Wang, Z.; Qi, Y.; Ding, C.; Fan, D.; Liu, G.; Zhao, Y.; Li, C., Insight into the charge transfer in particulate Ta3N5 photoanode with high photoelectrochemical performance. *Chemical Science* **2016,** *7* (7), 4391-4399.

45. Shi, C.; Billinge, S. J. L.; Puma, E.; Bang, S. H.; Bean, N. J. H.; de Sugny, J.-C.; Gambee, R. G.; Haskell, R. C.; Hightower, A.; Monson, T. C., Barium titanate nanoparticles: Short-range lattice distortions with long-range cubic order. *Phys. Rev. B* **2018,** *98* (8), 085421.

46. Yoon, K. H.; Chung, K. S., Photoelectrochemical effects of BaTiO3 thin film electrodes prepared by the sol-gel method. *Journal of Applied Physics* **1992,** *72* (12), 5743-5749.

47. Doughty, R. M.; Hodges, B.; Dominguez, J.; Han, R.; Zhao, Z.; Assavachin, S.; Osterloh, F. E., Fermi Level Pinning Controls Band Bending and Photochemical Charge Separation in Particles of n-SrTiO3, n-SrTiO3:Al, and n-GaAs:Te. *The Journal of Physical Chemistry C* **2020,** *124* (34), 18426-18435.

48. Doughty, R. M.; Chowdhury, F. A.; Mi, Z.; Osterloh, F. E., Surface photovoltage spectroscopy observes junctions and carrier separation in gallium nitride nanowire arrays for overall water-splitting. *The Journal of Chemical Physics* **2020,** *153* (14), 144707.

49. Cao, G., *Nanostructures and Nanomaterials: Synthesis, Properties and Applications*. World Scientific Publishing Company: 2011; p 63.

50. Kim, Y. S.; Kim, D. H.; Kim, J. D.; Chang, Y. J.; Noh, T. W.; Kong, J. H.; Char, K.; Park, Y. D.; Bu, S. D.; Yoon, J.-G.; Chung, J.-S., Critical thickness of ultrathin ferroelectric BaTiO3 films. *Applied Physics Letters* **2005,** *86* (10).